2012

Intrinsic defects in multiferroic $BiFeO_3$ and their effect on magnetism

Tula R. Paudel
University of Nebraska-Lincoln, tula.paudel@gmail.com

Sitaram S. Jaswal
University of Nebraska-Lincoln, sjaswal1@unl.edu

Evgeny Y. Tsymbal
University of Nebraska-Lincoln, tsymbal@unl.edu

Intrinsic defects in multiferroic $BiFeO_3$ and their effect on magnetism

Tula R. Paudel,* Sitaram S. Jaswal, and Evgeny Y. Tsymbal
Department of Physics and Astronomy, Nebraska Center for Materials and Nanoscience, University of Nebraska, Lincoln, Nebraska, 68588
(Received 30 November 2011; revised manuscript received 31 January 2012; published 14 March 2012)

We investigate the energetics of the intrinsic defects in bulk multiferroic $BiFeO_3$ and explore their implication for magnetization using a first-principles approach based on density functional theory. We find that the dominant defects in oxidizing (oxygen-rich) conditions are Bi and Fe vacancies and in reducing (oxygen-poor) conditions are O and Bi vacancies. The calculated carrier concentration shows that the $BiFeO_3$ grown in oxidizing conditions has *p*-type conductivity. The conductivity decreases with oxygen partial pressure, and the material becomes insulating with a tendency for *n*-type conductivity. We find that the Bi and Fe vacancies produce a magnetic moment of $\sim 1\mu_B$ and $5\mu_B$ per vacancy, respectively, for *p*-type $BiFeO_3$ and none for insulating $BiFeO_3$. O vacancies do not introduce any moment for both *p*-type and insulating $BiFeO_3$. Calculated magnetic moments due to intrinsic defects are consistent with those reported experimentally for bulk $BiFeO_3$.

DOI: 10.1103/PhysRevB.85.104409 PACS number(s): 71.55.−i, 75.85.+t, 61.72.J−, 72.80.Cw

I. INTRODUCTION

Multiferroic materials that simultaneously display magnetic and electric order have attracted significant interest due to their interesting physical properties that are promising for multifunctional device applications.[1–13] The magnetoelectric coupling between the electric and the magnetic degrees of freedom, where an electric (magnetic) polarization can be induced by a magnetic (electric) field, is especially exciting.[14,15] Magnetoelectric multiferroics allow the possibility of switching the magnetization with the electric field, which offers ample opportunity for information storage applications.[16,17]

$BiFeO_3$ (BFO) is a particular example of a single-phase multiferroic material that has recently attracted special attention due to its room temperature multiferroic properties.[3,18,19] Bulk BFO is antiferromagnetic with the Néel temperature $T_N = 643$ K[20] and ferroelectric with the Curie temperature $T_C = 1103$ K.[21] Theoretically predicted spontaneous polarization ($P_s \approx 100$–150 $\mu C/cm^2$)[22–24] has been found in thin films at room temperature.[3,18,25] Bulk BFO, however, exhibits relatively low polarization ($P_s \approx 5$–10 $\mu C/cm^2$).[26–28] Bulk BFO has the rhombohedrally distorted perovskite[29] structure, in which ionic sublattices are displaced relative to one another in the polar [111] direction, and the oxygen octahedra are rotated around the same [111] axis.[22] When grown as a thin film, BFO may have a monoclinic (BB or BB′) or a tetragonal ($P4mm$) structure, depending upon the strain imposed by the underlying substrate. For example, at room temperature, a BFO film grown on a highly mismatched $LaAlO_3$ substrate has a $P4mm$ structure,[30,31] that grown on $SrRuO_3/SrTiO_3$ (STO) is monoclinic,[32] and that grown on $LaNiO_3$ has a mixed phase of $R3c$ and $P4mm$.[33] At a higher temperature ($\sim$700 K), both a bulk single crystal and a thin-film sample undergo a structural phase transition to the orthorhombic and eventually ($\sim$1100 K) to the cubic perovskite.[32]

Bulk BFO exhibits a G-type antiferromagnetic order,[34] where the magnetic moment of each Fe cation is antiparallel to that of its nearest neighbors. The calculated magnetocrystalline anisotropy predicts that a preferred orientation of the Fe magnetic moments is perpendicular to the polar [111] direction.[35] A small canting of the Fe magnetic moments leads to a net magnetization of ~ 5 emu/cm^3. However, it was found that some thin films exhibit a very large saturation magnetization exceeding 70 emu/cm^3.[36] The origin of this large magnetization remains unclear.

Intrinsic point defects, especially oxygen vacancies V_O, have been proposed as a possible source of magnetization in BFO.[36] However, a comprehensive theoretical study to explore various possible point defects in BFO and their effect on magnetization is still lacking. Ju and Cai studied the electronic structure of oxygen vacancies and its effect on the dielectric properties of BFO.[37] Clark and Robertson studied their ionization energy.[38] Zhang *et al*. investigated energies of the formation of oxygen and cation vacancies and discussed their possible implications for the conductivity of BFO.[39] No preceding report considered the effects of individual point defects on the net magnetization of BFO. Ederer and Spaldin investigated the effect of oxygen vacancies on the weak ferromagnetism of BFO.[35] They found that oxygen vacancies lead to the formation of Fe^{2+} and can slightly alter magnetization.

In this paper, using a first-principles approach based on density functional theory (DFT), we explicitly calculate the energetics of possible intrinsic point defects in bulk BFO, i.e., cation and anion vacancies, as well as antisite defects. There are no high-symmetry vacant interstitial sites; hence, such defects are not considered. As all defects are treated on the same footing, we can quantitatively compare the tendency for the formation of various defects and their effects on properties of BFO. We find that the dominant defects in oxidizing conditions are Bi and Fe vacancies and in reducing conditions are O and Bi vacancies. The calculated carrier concentration shows that BFO grown in oxidizing conditions has *p*-type conductivity. The conductivity decreases with oxygen partial pressure, and the material becomes insulating with a tendency for *n*-type conductivity. We find that the Bi and Fe vacancies produce a magnetic moment of $\sim 1\mu_B$ and $5\mu_B$ per vacancy, respectively, for *p*-type BFO and none for insulating BFO. O vacancies do not introduce any moment for both *p*-type and insulating BFO. Calculated net magnetizations due to intrinsic defects are consistent with those reported experimentally for bulk BFO.[40,41]

The rest of the paper is organized as follows. First, we briefly describe our computational approach. Then we consider conditions for thermodynamic stability of the BFO compound based on the range of chemical potentials for constituent elements. We next discuss the formation of various point defects and their electronic structure. Then we address a possible modification to BFO magnetization due to coupling between the defects and the host magnetic Fe ion. Finally, we discuss the effect of the defects on the net magnetization of BFO and conclude the article.

II. COMPUTATIONAL METHODS

We use the DFT band structure approach as implemented in the Vienna *ab initio* simulation package (VASP).[42,43] The projected augmented wave (PAW) method is used to approximate the electron–ion potential.[44] To treat exchange and correlation effects, we use both the local density approximation (LDA)[45] and the semiempirical LDA + U method[46] within a rotationally invariant formalism[47] for a better description of the localized transition metal d electrons. Here, we choose $U - J = 3$ eV for the $3d$ orbitals of Fe atoms, because this value of U provides good thermodynamics for a range of binary and ternary oxides,[48] including Fe oxides, and it provides a reasonable magnetic structure.[49]

We construct an 80-atom supercell by doubling $R3c$ lattice vectors in all three directions. The G-type antiferromagnetic order of the original cell is maintained. Vacancy is created by removing an atom in the supercell. Similarly, an antisite defect (Fe_{Bi} and Bi_{Fe}) is created by substituting an atom of one type for that of another type. Then, we relax the ions in the supercell, keeping its shape fixed until the Hellman-Feynman forces are less than 0.01 eV/Å. In the calculation, we use a kinetic energy cutoff of 340 eV for the plane wave expansion of the PAWs[44] and $2 \times 2 \times 2$ Monkhorst-Pack grid of k points[50] for Brillouin zone integration. In all calculations, we turn on spin polarization and switch off all symmetries other than time reversal to allow for possible symmetry broken relaxation around the defect. We do not include the spin–orbit interaction in our calculations. The spin–orbit interaction results in energy corrections on the order of micro- to millielectron volts, whereas the energies we are dealing with here are on the order of electron volts. The spin–orbit interaction in conjunction with exchange coupling leads to the Dzyaloshinskii-Moriya interaction, which is responsible for weak ferromagnetism in some oxide materials, including BFO, where magnetization of $0.1\mu_B$ per unit cell[49] has been reported to be associated with this effect. Here, we neglect this contribution.

Various nonisovalent defects have different ionization levels. For example, V_{Bi} and V_{Fe} have three ionization levels, and V_O has two ionization levels. To create an ionized (charged) defect, we add electrons to or remove electrons from the system and include a compensating jellium background. Additional charge in the system introduces two complications. The first is the interaction between the charge and its image. We take this into account by adding to the total energy the screened Madelung energy of the point charge–image interaction in a lattice compensated by a jellium background, as suggested by Leslie and Gillan,[51] and the screened interaction between the delocalized part of the charge and its image due to Makov and Payne.[52] The dielectric constant that determines screening is calculated using density functional perturbation theory[53] as implemented in the VASP. The second complication is the arbitrary shift in total energy due to the additional charge in the system. We correct this shift by calculating a difference in the atomic sphere–averaged electrostatic potentials between the host and the charged system.[54] These corrections effectively remove the supercell size-dependent energy of a charged system[54,55] and effectively represent the energy of an infinite crystal with a single charge (dilute limit). This approach has been used in various oxide systems,[56–60] including spinels,[61] to calculate the formation enthalpy ΔH_f of the (charged) defect in dilute limit.

The formation enthalpy of various defects in the system are used to calculate their concentration at a given temperature in the dilute limit even if the supercell size used in the first-principles calculation is smaller to accommodate such dilute concentrations. We describe this approach in Sec. III C. In brief, we minimize the Gibbs free energy of a system with various defects as a function of the defect concentration. We then self-consistently find the defect concentration C_D, the Fermi energy E_F^{eq}, and the carrier concentration as functions of temperature.

III. RESULTS

A. Range of chemical potentials and stability of BFO

The enthalpy of the formation of BFO is defined with respect elements at ambient conditions as $H_f = E(\text{BFO}) - \mu^{el}{}_{Bi} - \mu^{el}{}_{Fe} - 3\mu^{el}{}_{O}$. However, solid BFO usually is the product of the high-temperature reaction between Fe_2O_3 and Bi_2O_3. Chemical potentials (μ) of Bi, Fe, and O elements in such a reaction are different from those of elemental Bi, Fe, and O (μ^{el}) by an amount $\Delta\mu$ such that $\mu = \mu^{el} + \Delta\mu$. There exists a certain region of chemical potentials in which pure BFO exists. This region is determined by the following conditions: $\Delta\mu_{Bi} + \Delta\mu_{Fe} + 3\Delta\mu_O \geqslant \Delta H_f$ (BFO), $2\Delta\mu_{Fe} + 3\Delta\mu_O \leqslant \Delta H_f$ (Fe_2O_3), and $2\Delta\mu_{Fe} + 3\Delta\mu_O \leqslant \Delta H_f$ (Bi_2O_3), where for convenience we set $\mu^{el} = 0$. The values of H_f for competing phases Bi_2O_3 and Fe_2O_3 here are taken from tabulated experimental values.[62] Solving these three relations, we eliminate $\Delta\mu_O$ and express the chemical potential of one of the cations in terms of the other (i.e., $\Delta\mu_{Fe}$ in terms of $\Delta\mu_{Bi,}$) to determine the diagram of stability. Using the correct values of H_f is crucial, because they directly affect the range of chemical potentials in which BFO is stable. Because the H_f values of competing phases are taken from experiments and atomic chemical potentials are fitted to produce such values, room for uncertainty in the calculated ranges of the chemical potentials is very small, including an error in calculating the total energy of BFO. Figure 1 shows the stability regions of different compounds against Bi and Fe chemical potentials. The stability region of BFO is indicated by shaded region. It is seen from Fig. 1 that $\Delta H_f(BFO)/2 \leqslant \Delta\mu_{Fe}$, $\Delta\mu_{Bi} \leqslant 0$, and -2.0 eV $\leqslant \Delta\mu_O \leqslant 0$. In the oxidizing (oxygen-rich) conditions ($\Delta\mu_O \approx 0$), $\Delta\mu_{Fe}$ and $\Delta\mu_{Bi}$ have a large negative value and represent the metal-poor conditions, whereas in the reducing (oxygen-poor) conditions ($\Delta\mu_O \approx$

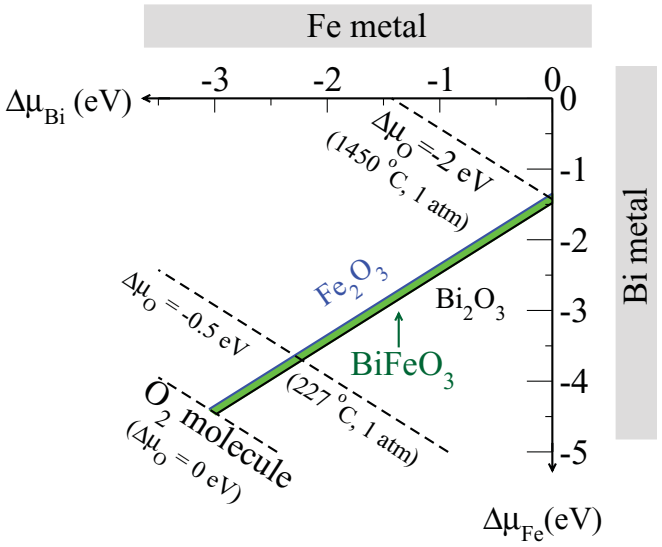

FIG. 1. (Color online) Stability regions of different compounds against Bi and Fe chemical potentials. The stability region of BFO is indicated by shaded region. The chemical potential isoline labeled "O_2 molecule" corresponds to the most oxidizing condition ($\Delta\mu_O = 0$), which reduces while going toward the origin. Other phases such as $Bi_2Fe_4O_9$, Fe_3O_4, and FeO do not change the BFO region of stability.

-2 eV), $\Delta\mu_{Fe}$ and $\Delta\mu_{Bi}$ have either zero or small negative values (Fig. 1) and represent metal-rich conditions.

Enthalpies of formation of competing phases such as Bi_2O_3, Fe_2O_3, Fe_3O_4, FeO, $Fe_4Bi_2O_9$, $Bi_4Fe_2O_9$, and O_2 molecules were calculated. The chemical potential of the oxygen molecule includes the corrections suggested in Ref. 59 that take into account a zero point energy, as well as the extra contribution required to fit the calculated heats of formation to the large data set of oxides.[48] The chemical potential of elemental Bi is calculated by fitting to the experimental heat of formation of Bi_2O_3.[62] The chemical potential of elemental Fe is the average chemical potential obtained by fitting to the experimental heat of formation of FeO, Fe_2O_3, and Fe_3O_4.[62]

The elemental chemical potentials of Fe and Bi represent the total energy of elemental solids, and the chemical potential of oxygen represents the energy of half the oxygen molecule. The formation energy calculations require the chemical potentials of the constituent elements of the compound. In LDA + U calculations, the same values of U for Fe in the metallic phase and for Fe in BFO are not expected to be very realistic.[59] We find that using the elemental chemical potentials obtained by fitting to the heat of the formation of competing phases provides the calculated heat of the formation of BFO, consistent with the experimental result.[63] Because the elemental chemical potentials are fitted to produce the heat of the formations of binary oxides, the relative stability of competing phases is also correct. The stability of competing phases directly affects the range of chemical potentials for which the compound of interest is stable.

In BFO, the calculated range of stability is narrow (the shaded area in Fig. 1), signifying that the heat of reaction between Bi_2O_3 and Fe_2O_3 is small and the compound is borderline. Nevertheless, no other phases limit the formation of BFO in very oxidizing conditions. However, the small enthalpy of the formation (-7.4 eV) of BFO limits its formation in very reducing conditions. As a result, the range of oxygen chemical potentials at which BFO is stable is relatively narrow (-2.0 eV $\leqslant \Delta\mu_O \leqslant 0$) compared to other perovskites, such as STO (-5.7 eV $\leqslant \Delta\mu_O \leqslant 0$) or LAO ($-6.0$ eV $\leqslant \Delta\mu_O \leqslant 0$). The existence of other phases, such as Fe_3O_4, $Bi_2Fe_4O_9$, and $Fe_2Bi_4O_9$, was found not to affect the stability of BFO.

The calculated oxygen chemical potential is translated into the set of temperature and pressure by using ideal gas as $\Delta\mu_O(T,P) = [H_0 + c_p(T - T_0) - TS_0 + Tc_p ln(T/T_0) + k_B T ln(P/P_0)]/2$ with $c_p = 3.5k_b$, where $k_b = 1.4 \times 10^{-23}$ $m^2kg^{-2}K^{-1}$ and tabulated values of oxygen at $T_0 =$ 298 K and $P_0 = 1$ atm are $H_0 = 8700$ $Jmol^{-1}$ and $S_0 =$ 205 $Jmol^{-1}K^{-1}$.[62] This translation is indicated in Fig. 1 by the dashed lines. The result $\Delta\mu_O = 0$ is virtually unachievable, because it corresponds to 2000 °C in temperature and 120 atm in pressure.

B. Formation and ionization of intrinsic point defects

The energy of formation of a defect D is the energy cost to add (remove) an atom of charge q to (from) an otherwise perfect host. Assuming thermal equilibrium between the host and the charge interchanging reservoirs that are characterized by the chemical potentials $\mu_{removed}$ and μ_{added} for removed and added atoms, respectively, the energy of defect formation is defined by $\Delta H_f(D,q) = E(D,q) - E_H + \mu_{removed} + \mu_{added} + qE_F$, where $E(D,q)$ is the energy of the host with the defect, E_H is the energy without the defect, and E_F is the electrochemical potential of the charge q. E_F is usually measured with respect to the host valence band maximum (VBM) E_V.

The charge transition energy between two charge states q and q' of a defect represents the energy required to ionize a defect in charge state q to the other charge state q'. This energy per unit charge is defined as $E(q/q') = [\Delta H_f(q) - \Delta H_f(q')]/(q' - q)$. This transition energy is independent of the chemical potentials (growth conditions) due to their cancelation. Shallow donors with transition levels closer to the conduction band minimum (CBM) and shallow acceptors with levels closer to the VBM are easy to ionize and contribute to the overall conductivity in the compound. Deep defects have transition energies deep in the band gap. Such defects primarily behave as traps for carriers.

Using the LDA + U method with $U - J = 3.0$ eV on the Fe-3d orbital, we find the band gap of BFO to be ~1.7 eV. This value is ~1 eV lower than the direct optical band gap of 2.74 eV measured experimentally.[63] Therefore, in our thermodynamic calculations that are used to determine the defect concentration, we assumed a rigid shift of 1 eV to the conduction band. We expect this shift to affect the behavior of shallow donor defects. Here, only the V_O donor level is deep with respect to the CBM. The upward shift of the conduction band further deepens the already-deep V_O level; however, its effect on the number of defects, as well as the conductivity, remains unchanged.

Figure 2 shows the formation energy of the most stable charge state of a defect as a function of the Fermi energy for one of the oxidizing and the most reducing conditions. In the oxidizing conditions, the formation enthalpy of cation

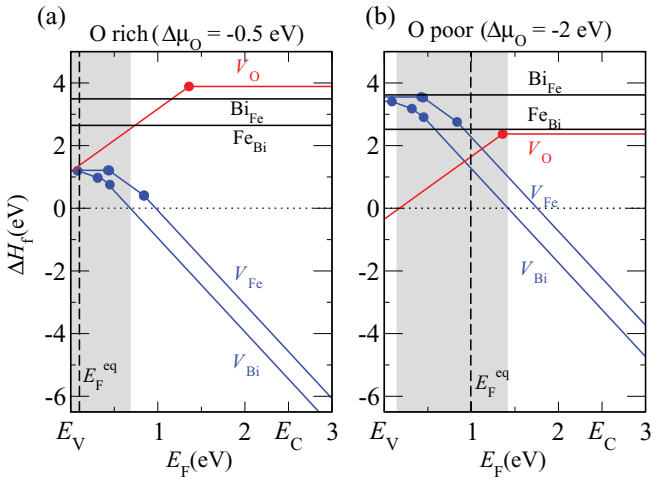

FIG. 2. (Color online) Enthalpy of the formation of various intrinsic defects as a function of the Fermi energy in the band gap of BFO for (a) oxygen-rich and (b) oxygen-poor conditions. Straight lines represent charge states of the defect, and break points—shown by solid circles—represent charge transition energy. Only the most stable charge state of a defect at a given Fermi energy is shown. E_V and E_C denote positions of the VBM and the CBM, respectively. The shaded regions show the accessible range of the Fermi energy.

vacancies is smaller than 1.1 eV. At the maximum possible oxidizing condition $\Delta\mu_O = 0$ eV, ΔH_f (V_{Bi}) drops to ~0.2 eV, whereas ΔH_f (V_O) increases to ~2.0 eV. The enthalpy of the formation of V_{Fe} is slightly larger than that of V_{Bi} but follows the similar trend. This indicates cation vacancies are the dominant defects in oxidizing conditions. This is consistent with V_O being unlikely to form in the oxidizing conditions, whereas V_{Bi} is likely to form, because Bi is known to be relatively volatile.[64] However, this contrasts with the relatively large energy of formation for the cation vacancy reported in Ref. 39. The difference mainly results from use of different atomic chemical potentials for Fe and Bi. The enthalpy of the formation of oxygen vacancy is also different; however, the difference is much smaller than that for cation vacancy. The small difference again comes from the use of different chemical potentials of oxygen. We include a correction in the oxygen chemical potential that comes partly from fitting it to a large set of the oxide enthalpy of formation and partly from zero point motion. These different values also affect the range of chemical potentials and contribute to differences mainly in reducing conditions. Furthermore, cation defects have small transition energies; therefore, they are easily ionized and produce holes rendering compound *p*-type. This is consistent with Ref. 39, because ionization energy is the energy difference between two charge states of defects, leaving behind the effects of chemical potentials at a given Fermi energy. Equilibrium Fermi energy E_F^{eq} in the system is determined by the charge neutrality condition. This is achieved either by having an equivalent number of free electrons and holes or by having free holes (electrons) and their traps. Deep localized defects such as oxygen vacancy (in BFO) trap the carriers (holes). Oxygen vacancies dominate over the cation vacancies only when the Fermi energy is shifted down toward the VBM, which may be achieved by doping with an external acceptor–type impurity, i.e., a dopant that creates holes in BFO. In this case, the E_F^{eq} of the defect-rich BFO can be pushed even farther below the VBM of the perfect BFO (down to −0.5 eV), because there is no defect that blocks the movement of the Fermi level. The ideal oxidizing condition of $\Delta\mu_O = 0$, corresponding to BFO/O_2 equilibrium, is physically unrealistic. Hence, we choose the oxidizing condition to be $\Delta\mu_O = -0.5$ eV, which is achievable in experiments using a variety of temperatures and pressures, e.g., $T = 500\,^\circ$C and $P = 1$ atm. According to the ideal gas law, oxygen chemical potential is a function of temperature and pressure (Sec. III A). We fix temperature and vary pressure, and vice versa, to achieve the same chemical potential. Furthermore, at such a temperature as 500 °C, the thermal equilibrium between constituent ions in BFO is expected even at ambient pressure. To achieve $\Delta\mu_O = 0$ eV at ambient pressure, we need to decrease the temperature to 10 K. At such a temperature, no reaction occurs, let alone thermal equilibrium.

In the reducing conditions, the energy of formation is so high that both anion and cation vacancies are difficult to form. When under electron doping the Fermi level is pushed toward the CBM, the formation energy of the cation vacancy tends to decrease. The number of acceptor defects increases, releasing holes and compensating for the effect of doping that makes the compound insulating. However, the movement of the Fermi level is limited to a narrow range of 1.25 eV (shown by the shaded region in Fig. 2) around E_F^{eq}, much narrower than the band gap of 2.7 eV. When the Fermi level is moved beyond this range, the compound becomes unstable due to spontaneous formation of large number of defects. For example, at O-poor conditions [Fig. 2(b)], oxygen vacancies start forming spontaneously when the Fermi level falls to 0.1 eV and Bi vacancies start forming spontaneously when it rises above 1.4 eV, with both destabilizing BFO.

The energy of the formation of a defect depends partly on the local bonding environment. In BFO, because the Fe-O bond length of 1.93 Å is shorter than the Bi-O bond length of 2.31 Å, the formation of the Bi vacancy is easier than the formation of the Fe vacancy. This is consistent with our observation that ΔH_f (V_{Fe}) is higher than ΔH_f (V_{Bi}). Further antisite defects are unlikely due to a large difference in their radii (the Bi^{3+} ionic radius of 1.17 Å is ~32% larger than that of the Fe^{3+} ionic radius), consistent with the large heat of formation of the antisite defects. We find similar behavior of point defects in other perovskites, such as LAO, STO, and BTO, viz. vacancies that have lower formation energy compared to antisite defects. However, V_O can be formed in LAO, STO, and BTO under much larger reducing conditions, because they exist in more reducing conditions ($\Delta\mu_O < -5$ eV) compared to BFO ($\Delta\mu_O \approx -2$ eV). Consequently, calculated V_O formation energy is much higher in BFO compared to that in other perovskites, including LAO (~0.4 eV), STO (~0.1 eV), and BTO (~0.1 eV).

C. Defect concentrations and oxygen chemical potentials

We calculate the number of defects $C_D(T,\mu_{O2})$ by minimizing the Gibbs free energy. The latter is given by $G(D) = \Delta H_f(D) - TS$, with S being the entropy due to different ways of arranging the defects among the available

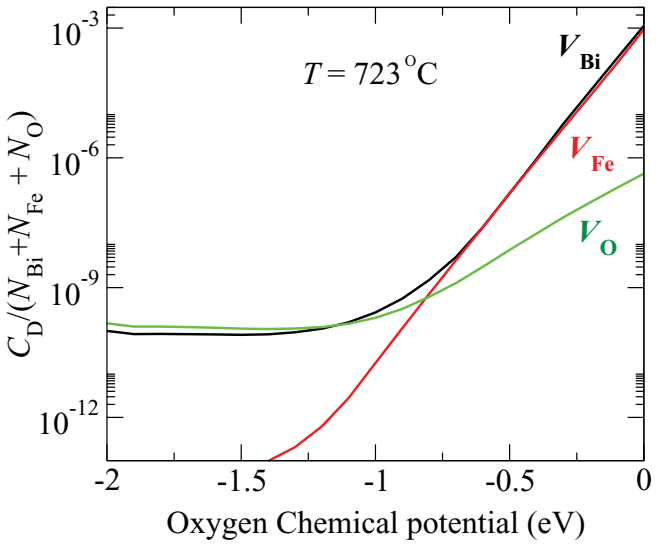

FIG. 3. (Color online) The relative number of defects as a function of the oxygen chemical potential at ambient pressure and 723 °C.

sites N, such that $C_D = N\exp[-\Delta H_f(D)/k_B T]$. Here, $\Delta H_f(D)$ depends upon the growth conditions μ_O and the Fermi energy E_F, where E_F depends on the number of carriers, some of which are coming from ionized defects. We then self-consistently calculate E_F^{eq} and C_D at a given temperature,[65] assuming an overall charge neutrality.

The defect concentration increases exponentially with temperature. Thus, it is more interesting to compare the defect concentration calculated at different $\Delta\mu_O$ values, because it effectively characterizes the number of defects in a sample grown under different growth conditions. In Fig. 3, we plot the number of defects as a function of the oxygen chemical potential at a given temperature. Again, $\Delta\mu_O = 0$ represents most possible oxidizing condition, and increasingly negative $\Delta\mu_O$ represents various reducing conditions. It is seen from Fig. 3 that the overall number of defects decreases in reducing conditions and the dominant defect changes from cation vacancies in the oxidizing conditions to the oxygen and Fe vacancies in the reducing conditions. Considering that cation vacancies are shallow—and hence hole producers—and oxygen vacancies are deep and act merely as hole traps, the BFO compound, especially when grown under oxidizing conditions, behaves as a p-type conductor, as seen experimentally.[66] Conductivity of BFO decreases in reducing conditions, where it essentially behaves as an insulator. This behavior is typical of p-type oxides mainly because hole producer defects such as cation vacancies are easier to form; at the same time, hole killer defects such as oxygen vacancies are less easy to form in oxidizing conditions. The large number of cation vacancies in this case does not necessarily mean large hole conductivity, because we expect a very low hole mobility as a result of the essentially flat valence band formed from the relatively localized Fe-3d band. Overall, our calculation indicates that the sample grown in oxidizing conditions is expected to be more conductive, because of cation vacancies, than the sample grown in reducing conditions. This prediction is consistent with the results of Ref. 67, where samples annealed in oxygen are found to have larger conductivity than samples annealed in vacuum.

D. Electronic structure of point defects and their effect on magnetization

1. Cation vacancies

Bi vacancies introduce three holes in the system with the possibility of carrier-induced ferromagnetism. The point group symmetry of Bi in BFO is C_{3v}, despite Bi being bonded with six oxygen atoms. One set of three Bi-O bonds has a bond length of 2.31 Å, and another set of three Bi-O bonds has a bond length of 2.41 Å. In this symmetry, the dangling bond-related state splits into $a^2e_g{}^4$ (superscript numbers represent the occupation of the level, including spin polarization). Due to relaxation, when symmetry is lowered to C_1, the e-like state splits into two a-like states, as seen from Fig. 4(a). In the literature, Bi has sometimes been treated as having approximate O_h symmetry, reflecting the small difference between two sets of Bi-O bonds. In terms of O_h symmetry, the dangling bond-related state splits according to $a^2t_{2g}{}^6e_g{}^4$. Due to relaxation, the e-like state splits into two a-like states, and analysis becomes the same as in the case of C_{3v} point group symmetry.

In the case of charge-neutral Bi vacancy, the lower a-like state is half filled, whereas the upper a-like state is empty; in addition, the Fermi level passes through the middle of the lower a-like state. The electron in the lower a-like state couples with one of the 3d electrons in Fe with the spin in the same direction, producing a net magnetization of $1\mu_B$ per vacancy. In Fig. 4(b), we show this orbital and the possible coupling mechanism between Bi vacancy and Fe.

In the case of Bi vacancy in the 1^- charge state, the lower a_1-like state is filled with two spin-up and spin-down electrons, resulting in no net magnetization. In the 2^- charge state, the upper a_1-like state has one electron, resulting in the magnetic moment of $1\mu_B$ per vacancy. In the 3^- charge state, the upper a_1-like state has two spin-up and spin-down electrons, resulting in no magnetic moment. However, the charge-neutral V_{Bi} is

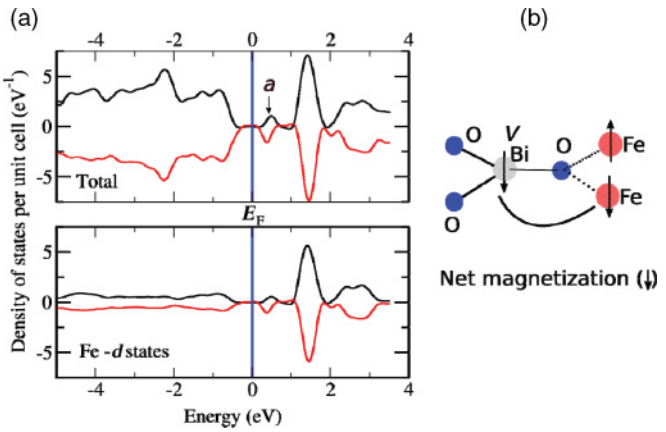

FIG. 4. (Color online) Calculated density of states (DOS) as a function of energy for bulk BFO containing (a) charge-neutral Bi vacancies and (b) the coupling mechanism between the Bi vacancy and the host Fe atom in BFO. In (a), the top panel shows the total DOS, and the bottom panel shows the Fe-3d partial DOS. An arrow indicates the a-like vacancy state.

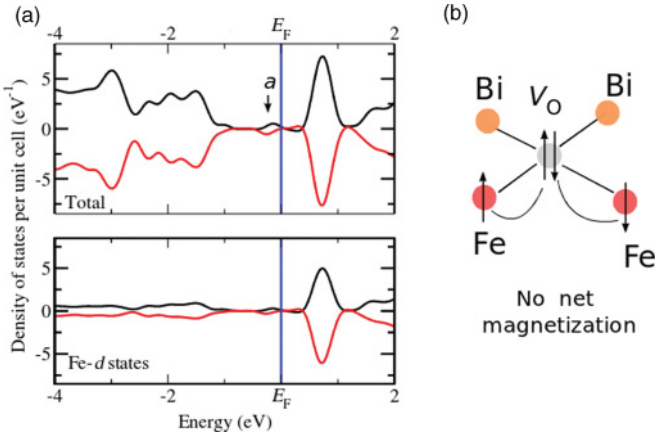

FIG. 5. (Color online) Calculated DOS as a function of energy for bulk BFO containing (a) O vacancies and (b) the coupling mechanism between the O vacancy and the host Fe atom in BFO. In (a), the top panel shows the total DOS, and the bottom panel shows the sum of the Fe-d partial DOS. An arrow indicates the *a*-like vacancy state.

dominant due to the *p*-type nature of the compound; thus, no net magnetization in BFO is expected in this case.

In the case of Fe vacancy, removing a Fe atom results in net magnetization of $\sim 5\mu_B$ per vacancy originating from the difference in magnetic moments between the two adjacent planes with the G-type antiferromagnetic arrangement of spins.

2. Oxygen vacancies

The charge-neutral O vacancy leaves behind two uncompensated electrons in the system. Strictly speaking, the oxygen point group symmetry in BFO is C_1. In this symmetry, the *a*-like dangling bond-related state lies in the gap, as seen from Fig. 5(a). (Note the two unoccupied states in the gap.) Another way to consider this is to start from oxygen having approximate T_d symmetry, in which the dangling bond-related state splits into $a^2 {t_{2g}}^6$ states. Lowering the symmetry to C_{2V} leads to the ${t_{2g}}^6$ state splitting into a^2 and ${e_g}^4$ states. Additional lowering of the symmetry around the vacancy site to C_1 further splits the e_g-like orbital into two *a*-like orbitals. Out of these two orbitals, the lower one lies in the valence band and the higher one lies in the band gap with two spin-up and spin-down electrons. The spin-up electron couples with the spin-up Fe electron, and the spin-down electron couples with the spin-down Fe electron, resulting in the same change in either spin channel. Hence, no net magnetization appears in the compound, as shown in Fig. 5(b). In the 1^+ charge state, V_O carries a moment of $1\mu_B$, but this state is unstable; in the 2^+ charge state, V_O does not carry a significant moment.

3. Antisite defects

Antisite substitutions of Fe on Bi and Bi on Fe introduce a magnetic moment of $5\mu_B$ per defect as they create imbalance of the spin moment in the plane with respect to the adjacent plane in the G-type antiferromagnetic lattice of BFO. In reality, such defects are expected to distribute randomly in either plane, canceling each other's moments and resulting in no net magnetization.

4. Net magnetization

We define the net magnetization as $M = \sum_d C(d)m(d)$, where $C(d)$ is the concentration of defects and $m(d)$ is the magnetic moment per defect. When we introduce two Bi vacancies in our supercell calculation, the case in which the net magnetic moment of the system doubles is found to be more stable, signaling that moments due to V_{Bi} align ferromagnetically. Defect concentration used for the determination of ferromagnetic coupling is larger than that predicted by the enthalpy of formation. Similarly, for Fe vacancies, two defects in a ferromagnetic layer create the net moment, which is equivalent to twice the local moment of one Fe atom. However, we find that two Fe vacancies lying in two antiferromagnetically aligned planes produce no net magnetic moment. Thus, assuming that Fe vacancies are randomly distributed leads to virtually no net magnetization in bulk BFO. As we have already discussed, oxygen vacancies in the charge-neutral state also do not produce any moment.

Using the number of defects shown in Fig. 3 and the magnetic moment they introduce in the system, we calculate the net magnetization of bulk BFO. The result is as follows: ~ 2 emu/g ($0.0016\mu_B$ per formula unit, 0.25 emu/cm^3) at oxidizing conditions ($\Delta\mu_{O2} = -0.2$ eV). Here, we used the density of BFO as 8.34 g/cm^3. This very small magnetization is similar to that of 0.14 emu/g found in BFO grown using a wet chemical method.[40] We predict no net magnetization for BFO grown in reducing conditions, which is consistent with reduced magnetization in bulk ceramics samples grown using solid state reaction and sintered in vacuum, Ar, or N.[41] Overall, bulk samples grown using various techniques do not show sizable magnetization, which is in agreement with our defect calculations. The other possibility of inducing ferromagnetism—such as defect-induced noncollinearity changing magnetic ordering of the Fe sublattice, defect paring, and clustering—even though not considered in our calculation, is expected to be small given the dilute concentration of defects and large Néel temperature of 643 K in BFO. Furthermore, the long-wavelength spin density wave generated by spin canting out of the rotation plane of the antiferromagnetic cycloidal order, as seen in neutron scattering, also results in a small average local magnetization of $\sim 0.06\mu_B$ per Fe atom.[36] This effect is, however, not considered within our model.

Surprisingly, some thin-film samples have shown a large magnetization—up to $0.5\mu_B$ per Fe.[36] The effects of strain and/or interfaces have been put forward to explain this phenomenon.[68] However, thin-film growth is guided by complicated dynamic processes rather than thermodynamic equilibrium, which may contribute to the differences between bulk and thin-film samples, as well as those between thin films grown at different conditions. Given the stability of BFO in a rather narrow window on the stability diagram (Fig. 1), film growth may be accompanied by the formation of second phases, which may introduce magnetism in the system. Thorough structural characterization is critical to avoid these artifacts in experiments. Furthermore, the dependence of magnetization on film thickness[3,69] points toward the role of strain. In particular, tensile strain would decrease the energy of formation of V_{Bi} and V_{Fe} and produce a large number of defects. However, the large magnetization of $\sim 0.5\mu_B$

per Fe requires ∼5% V_{Bi} or 1% V_{Fe} with respect to the total number of sites. In the case of Fe vacancies, there are further constraints: they have to be formed entirely in the ferromagnetically aligned planes, which seems unlikely. In any case, such a high vacancy concentration should be detectable in experiments.

IV. CONCLUSIONS

We have investigated energetics of the intrinsic defects in bulk multiferroic BFO. We demonstrated that cation vacancies are dominant defects when the sample is grown under oxidizing conditions with no barrier for *p*-type doping or moving the Fermi level well below the VBM by applying an external field. Only when the Fermi level lies well below VBM do oxygen vacancies start appearing in a comparable amount with cation vacancies. The number of oxygen vacancies has a slight edge over the number of cation vacancies for the compound grown at reducing conditions; however, the overall concentration of either defect remains very small, rendering a compound insulating. Oxygen vacancy is found to create a deep defect level that traps holes rather than generating electrons, whereas the cation vacancies are rather shallow and generate holes.

We found that the charge-neutral Bi vacancies introduce an unpaired electron that couples with the Fe-3*d* electron, changing its local moment and resulting in net magnetization. Each Bi vacancy, when the Fermi level is close to VBM, as in the oxidizing conditions, produces a magnetic moment of $\sim 1\mu_B$ per vacancy, whereas each Fe vacancy produces a magnetic moment of $\sim 5\mu_B$ per vacancy. The magnetic moments due to Bi vacancies are aligned ferromagnetically and thus contribute to net magnetization, whereas the magnetic moments due to Fe vacancies may be aligned both ferromagnetically and antiferromagnetically and on average do not contribute to net magnetization. Oxygen vacancies do not introduce any magnetism in either growth condition. Due to point defects, BFO grown under the oxidizing conditions and high temperatures may show a small magnetization of ∼2 emu/cm^3, whereas BFO grown in reducing conditions is predicted to show no magnetization because of the relatively small number of defects. Thin-film BFO, which is usually strained, in principle can have a large number of cation vacancies due to the vacancy formation energy decreasing with the elongating bond, especially because of tensile strain. This would affect the stoichiometry of the compound due to Bi and Fe vacancies. However, producing a large magnetization of ∼70 emu/cm^3 ($\sim 0.5\mu_B$ per Fe) seen in some experiments requires a concentration of Bi point defects (∼5%). Such a sizable concentration of defects could be detected experimentally.

ACKNOWLEDGMENTS

This work was supported by the National Science Foundation (Grant Nos. EPS-1010674 and DMR-0906443). Computations were performed utilizing the Holland Computing Center of the University of Nebraska.

*tula.paudel@gmail.com

[1] G. A. Smolenskii and I. E. Chupis, Sov. Phys. Usp. **25**, 475 (1982).
[2] H. Schmid, Ferroelectrics **162**, 317 (1994).
[3] J. Wang, J. B. Neaton, H. Zheng, V. Nagarajan, S. B. Ogale, B. Liu, D. Viehland, V. Vaithyanathan, D. G. Schlom, U. V. Waghmare, N. A. Spaldin, K. M. Rabe, M. Wuttig, and R. Ramesh, Science **299**, 1719 (2003).
[4] M. Fiebig, J. Phys. D **38**, R123 (2005).
[5] N. A. Spaldin and M. Fiebig, Science **309**, 391 (2005).
[6] W. Eerenstein, N. D. Mathur, and J. F. Scott, Nature **442**, 759 (2006).
[7] S.-W. Cheong and M. Mostovoy, Nat. Mater. **6**, 13 (2007).
[8] R. Ramesh and N. A. Spaldin, Nat. Mater. **6**, 21 (2007).
[9] L. W. Martin, S. P. Crane, Y.-H. Chu, M. B. Holcomb, M. Gajek, M. Huijben, C.-H. Yang, N. Balke, and R. Ramesh, J. Phys. Condens. Matter **20**, 434220 (2008).
[10] D. Khomskii, Physics **2**, 20 (2009).
[11] K. F. Wang, J.-M. Liu, and Z. F. Ren, Adv. Phys. **58**, 321 (2009).
[12] J. P. Velev, S. S. Jaswal, and E. Y. Tsymbal, Phil. Trans. R. Soc. A **369**, 3069 (2011); J. P. Velev, P. A. Dowben, E. Y. Tsymbal, S. J. Jenkins, and A. N. Caruso, Surf. Sci. Rep. **63**, 400 (2008).
[13] J. Ma, J. Hu, Z. Li, and C.-W. Nan, Adv. Mater. **23**, 1062 (2011).
[14] T. Kimura, T. Goto, H. Shintani, K. Ishizaka, T. Arima, and Y. Tokura, Nature **426**, 55 (2003).
[15] T. Lottermoser, T. Lonkai, U. Amann, D. Hohlwein, J. Ihringer, and M. Fiebig, Nature **430**, 541 (2004).
[16] C. J. Fennie and K. M. Rabe, Phys. Rev. B **68**, 184111 (2003).
[17] Y.-H. Chu, L. W. Martin, M. B. Holcomb, and R. Ramesh, Mater. Today **10**, 16 (2007).
[18] H. W. Jang, S. H. Baek, D. Ortiz, C. M. Folkman, R. R. Das, Y. H. Chu, P. Shafer, J. X. Zhang, S. Choudhury, V. Vaithyanathan, Y. B. Chen, D. A. Felker, M. D. Biegalski, M. S. Rzchowski, X. Q. Pan, D. G. Schlom, L. Q. Chen, R. Ramesh, and C. B. Eom, Phys. Rev. Lett. **101**, 107602 (2008).
[19] T. Zhao, A. Scholl, F. Zavaliche, K. Lee, M. Barry, A. Doran, M. P. Cruz, Y. H. Chu, C. Ederer, N. A. Spaldin, R. R. Das, D. M. Kim, S. H. Baek, C. B. Eom, and R. Ramesh, Nat. Mater. **5**, 823 (2006).
[20] P. Fischer, M. Polomska, I. Sosnowska, and M. Szymanski, J. Phys. C **13**, 1931 (1980).
[21] G. A. Smolenskii, V. Isupov, A. Agranovskaya, and N. Kranik, Sov. Phys. Solid State **2**, 2651 (1961).
[22] J. B. Neaton, C. Ederer, U. V. Waghmare, N. A. Spaldin, and K. M. Rabe, Phys. Rev. B **71**, 014113 (2005).
[23] P. Ravindran, R. Vidya, A. Kjekshus, H. Fjellvåg, and O. Eriksson, Phys. Rev. B **74**, 224412 (2006).
[24] C. Ederer and N. Spaldin, Phys. Rev. Lett. **95**, 257601 (2005).
[25] J. X. Zhang, Q. He, M. Trassin, W. Luo, D. Yi, M. D. Rossell, P. Yu, L. You, C. H. Wang, C. Y. Kuo, J. T. Heron, Z. Hu, R. J. Zeches, H. J. Lin, A. Tanaka, C. T. Chen, L. H. Tjeng, Y.-H. Chu, and R. Ramesh, Phys. Rev. Lett. **107**, 094115 (2011).

[26] A. K. Pradhan, K. Zhang, D. Hunter, J. B. Dadson, G. B. Loiutts, P. Bhattacharya, R. Katiyar, J. Zhang, D. J. Sellmyer, U. N. Roy, Y. Cui, and A. Burger, J. Appl. Phys. **97**, 093903 (2005).
[27] Y. P. Wang, G. L. Yuan, X. Y. Chen, J.-M. Liu, and Z. G. Liu, J. Phys. D **39**, 2019 (2006).
[28] J. Teague, Solid State Comm. **8**, 1073 (1970).
[29] C. Michel, Solid State Comm. **7**, 701 (1969).
[30] H. Béa, B. Dupé, S. Fusil, R. Mattana, E. Jacquet, B. Warot-Fonrose, F. Wilhelm, A. Rogalev, S. Petit, V. Cros, A. Anane, F. Petroff, K. Bouzehouane, G. Geneste, B. Dkhil, S. Lisenkov, I. Ponomareva, L. Bellaiche, M. Bibes, and A. Barthélémy, Phys. Rev. Lett. **102**, 217603 (2009).
[31] Z. Chen, L. You, C. Huang, Y. Qi, J. Wang, T. Sritharan, and L. Chen, Appl. Phys. Lett. **96**, 252903 (2010).
[32] R. Palai, R. S. Katiyar, H. Schmid, P. Tissot, S. J. Clark, J. Robertson, S. A. T. Redfern, G. Catalan, and J. F. Scott, Phys. Rev. B **77**, 014110 (2008).
[33] Q. He, Y.-H. Chu, J. T. Heron, S. Y. Yang, W. I. Liang, C. Y. Kuo, H. J. Lin, P. Yu, C. W. Liang, R. J. Zeches, W. C. Kuo, J. Y. Juang, C. T. Chen, E. Arenholz, A. Scholl, and R. Ramesh, Nat. Comm. **2**, 225 (2011).
[34] S. V. Kiselev, R. P. Ozerov, and G. S. Zhdanov, Sov. Phys. Dokl. **7**, 742 (1963).
[35] C. Ederer and N. A. Spaldin, Phys. Rev. B **71**, 224103 (2005).
[36] J. Wang, A. Scholl, H. Zheng, S. B. Ogale, D. Viehland, D. G. Schlom, N. A. Spaldin, K. M. Rabe, M. Wuttig, L. Mohaddes, J. Neaton, U. Wagmare, T. Zhao, R. Ramesh, W. Eerenstein, F. D. Morrison, J. Dho, M. G. Blamire, J. F. Scott, and N. D. Mathur, Science **307**, 1203 (2005).
[37] S. Ju and T.-Y. Cai, Appl. Phys. Lett. **95**, 231906 (2009).
[38] S. J. Clark and J. Robertson, Appl. Phys. Lett. **94**, 022902 (2009).
[39] Z. Zhang, P. Wu, L. Chen, and J. Wang, Appl. Phys. Lett. **96**, 232906 (2010).
[40] S. M. Selbach, M.-A. Einarsrud, T. Tybell, and T. Grande, J. Am. Ceram. Soc. **90**, 3430 (2007).
[41] F. Huang, X. Lu, Z. Wang, W. Lin, Y. Kan, H. Bo, W. Cai, and J. Zhu, Appl. Phys. A **97**, 699 (2009).
[42] G. Kresse and D. Joubert, Phys. Rev. B **59**, 1758 (1999).
[43] G. Kresse and J. Furthmuller, Phys. Rev. B **54**, 11169 (1996).
[44] P. E. Blöchl, Phys. Rev. B **50**, 17953 (1994).
[45] J. P. Perdew and A. Zunger, Phys. Rev. B **23**, 5048 (1981).
[46] V. I. Anisimov, F. Aryasetiawan, and A. I. Lichtenstein, J. Phys. Condens. Matter **9**, 767 (1997).
[47] S. L. Dudarev, G. A. Botton, S. Y. Savrasov, C. J. Humphreys, and A. P. Sutton, Phys. Rev. B **57**, 1505 (1998).
[48] V. Stevanovi, X. Zhang, S. Lany, and A. Zunger (accepted by Phys. Rev. B, 2011).
[49] C. Ederer and N. A. Spaldin, Phys. Rev. B **71**, 060401(R) (2005).
[50] H. Monkhorst and J. Pack, Phys. Rev. B **13**, 5188 (1976).
[51] M. Leslie and N. J. Gillan, J. Phys. C **18**, 973 (1985).
[52] G. Makov and M. C. Payne, Phys. Rev. B **51**, 4014 (1995).
[53] S. Baroni and R. Resta, Phys. Rev. B **33**, 7017 (1986).
[54] S. Lany and A. Zunger, Phys. Rev. B **78**, 235104 (2008).
[55] S. Lany and A. Zunger, Model. Simulat. Mater. Sci. Eng. **17**, 084002 (2009).
[56] S. Lany and A. Zunger, Phys. Rev. Lett. **106**, 069601 (2011).
[57] H. Raebiger, S. Lany, and A. Zunger, Nature **453**, 763 (2008).
[58] S. Lany and A. Zunger, Phys. Rev. B **80**, 085202 (2009).
[59] S. Lany, Phys. Rev. B **78**, 245207 (2008).
[60] J. Osorio-Guillen, S. Lany, and A. Zunger, Phys. Rev. Lett. **100**, 036601 (2008).
[61] T. R. Paudel, A. Zakutayev, S. Lany, M. D'Avezac, and A. Zunger, Adv. Funct. Mater. **21**, 4493 (2011).
[62] D. Wagman, *The NBS Tables of Chemical Thermodynamic Properties: Selected Values for Inorganic and C1 and C2 Organic Substances in SI Units* (American Chemical Society and American Institute of Physics for the National Bureau of Standards, New York, 1982).
[63] J. F. Ihlefeld, N. J. Podraza, Z. K. Liu, R. C. Rai, X. Xu, T. Heeg, Y. B. Chen, J. Li, R. W. Collins, J. L. Musfeldt, X. Q. Pan, J. Schubert, R. Ramesh, and D. G. Schlom, Appl. Phys. Lett. **92**, 142908 (2008).
[64] A. Garg, S. Dunn, and Z. H. Barber, Integrated Ferroelectrics Int. J. **31**, 13 (2000).
[65] K. Biswas and S. Lany, Phys. Rev. B **80**, 115206 (2009).
[66] A. S. Poghossian, H. V. Abovian, P. B. Avakian, S. H. Mkrtchian, and V. M. Haroutunian, Sensor Actuator B Chem. **4**, 545 (1991).
[67] Z. Dai and Y. Akishige, J. Phys. D **43**, 445403 (2010).
[68] P. Yu, J. S. Lee, S. Okamoto, M. D. Rossell, M. Huijben, C. H. Yang, Q. He, J. X. Zhang, S. Y. Yang, M. J. Lee, Q. M. Ramasse, R. Erni, Y. H. Chu, D. A. Arena, C. C. Kao, L. W. Martin, and R. Ramesh, Phys. Rev. Lett. **105**, 027201 (2010).
[69] Y. Wang, Q.-H. Jiang, H.-C. He, and C.-W. Nan, Appl. Phys. Lett. **88**, 142503 (2006).